Research Article Vol. 59, No. 19 / 1 July 2020 / Applied Optics 5851

applied optics

Digital holographic interferometry investigation of liquid hydrocarbon vapor cloud above a circular well

DIGVIJAY SHUKLA AND PRADIPTA K. PANIGARHI*

Mechanical Engineering Department, Indian Institute of Technology Kanpur, Kanpur-208016, India
**Corresponding author: panig@iitk.ac.in*

Received 14 April 2020; revised 26 May 2020; accepted 27 May 2020; posted 28 May 2020 (Doc. ID 394874); published 1 July 2020

The current study investigates evaporation of liquid hydrocarbons from a circular well cavity of small depth. Gravimetric analysis is performed to measure the evaporation rate and digital holographic interferometry is used for the measurement of normalized mole fraction profile inside the vapor cloud above the well. Phase unwrapping has been implemented to obtain continuous phase distribution in the image plane. The Fourier–Hankel tomographic inversion algorithm is implemented to obtain the refractive index change distribution inside the object plane, i.e., vapor cloud. Four liquid hydrocarbons, i.e., pentane, hexane, cyclohexane, and heptane, are studied. The radius of circular well cavities is varied in the range of 1.5 to 12.5 mm. Results using a quasi-steady, diffusion-controlled model are compared with the experimental evaporation rate. Measured evaporation rates are higher than the diffusion-limited model calculation for all working fluids and well sizes. This difference is attributed to natural convection occurring inside the vapor cloud due to the density difference between the gas–vapor mixture and the surrounding air. Holographic analysis confirms the presence of natural convection by revealing the formation of a flat disk-shaped vapor cloud above the well surface. Experimentally obtained vapor cloud shape is different from the hemispherical vapor cloud obtained using the pure diffusion-limited evaporation model. The gradient of vapor mole fraction at the liquid–vapor interface is higher compared to that of the diffusion-limited model because of the additional transport mechanism due to natural convection. Transient analysis of the vapor cloud reveals time invariant overall shape of the vapor cloud with a reduction in average magnitude of vapor concentration inside the vapor cloud during evaporation. The existing correlation for sessile droplet cannot successfully predict the evaporation rate from a liquid well. A new correlation is proposed for evaporation rate prediction, which can predict the evaporation rate within a root mean square error of 5.6% for a broad size range of well cavity.

https://doi.org/10.1364/AO.394874

1. INTRODUCTION

Evaporation of small volume liquid well is observed in many applications, such as heat pipes [1], microreactors for chemical synthesis [2], microarray technologies for point of care clinical diagnostics [3], DNA sequencing for biological lab-on-chip applications [3], solid-state sensors [4], vapor bubbles in channel [5], organic light-emitting diode fabrication and pattern writing for color filters [6], etc. The advantages of a small-scale system is a lower sample cost and faster response. However, loss of liquid due to evaporation and permeation can be a concern for small volume liquid well systems. For instance, open liquid–air interface is prone to a high evaporation rate due to the surrounding conditions and reservoir geometry. Erroneous design of devices with a liquid well can lead to unsatisfactory performance. For example, a high concentration of solute in an open channel microreactor due to uncontrolled evaporation can lead to complete failure of the system. To overcome this limitation, several attempts have been made in the literature to control the evaporation from microreservoirs, such as placing a solid lid [7] and covering the liquid–air interface with an oil/organic liquid [8]. Several attempts have been made to understand the physical processes related to liquid evaporation of small volume. Most of the studies have been carried out to understand the evaporation process of liquid from sessile [9,10] and pendant droplets [11]. Limited studies are available on evaporation from microliter/nanoliter well cavities.

Previous studies [12,13] have reported correlation for evaporation rate estimation of a sessile droplet. However, no correlation is available for the prediction of evaporation from a liquid well. Marie *et al.* used digital holography for evaporation rate measurement of droplets [14]. Hjelt *et al.* used fluorescence microscopy for evaporation rate measurement of sub-nanoliter wells [15]. Chen *et al.*studied the evaporation of a liquid from

a nanoliter well and reported the interaction of liquid meniscus with the sidewall of the well [6]. Lynn *et al.* presented the meniscus shape evolution and instantaneous evaporation rate of water evaporating from contracting and expanding circular microreservoirs by the combined geometric/computational fluid dynamics model [16]. Various available techniques such as confocal microscopy/interference contrast microscopy [15,17] suffer from poor resolution near the sidewall. Hydrocarbons such as pentane, hexane etc., have very small contact angle due to low surface tension which further restricts the use of these techniques to accurately measure the evolution of meniscus. Therefore, experimental measurement of the evaporation rate from a liquid well requires an alternative approach from that of droplets. The present study uses direct measurement of the evaporation rate from a liquid well using gravimetric analysis, which does not require interface tracking for evaporation rate calculation.

In the case of liquid evaporating from a circular well cavity, liquid is surrounded by the well boundary and evaporation phenomenon is expected to be different from that of a sessile or pendant droplet. As evaporation takes place from the well cavity, the liquid–vapor interface moves away from the outlet boundary of the reservoir. The vapor cloud outside the well region can affect the vapor distribution inside the well region and ultimately the vapor concentration gradient at the liquid–vapor interface. Pradhan and Panigrahi investigated the influence of an adjacent droplet on liquid convection inside an evaporating droplet of binary mixture and reported that the presence of an adjacent droplet leads to asymmetric evaporative flux distribution on the droplet surface due to the influence of the neighboring droplet on the free stream mass fraction [18]. Subsequently, Pradhan and Panigrahi reported the effect of a neighboring liquid droplet on convection inside a liquid droplet inside a microchannel using micro- particle image velocimetry technique [19]. These studies indicate that the evaporation rate of one droplet is affected by the adjacent droplet through vapor cloud interactions. The vapor cloud above the well can interact with the vapor cloud from the neighboring well in multi-reservoir configuration. The vapor phase transport can play a significant role in control of evaporation of systems having multiple reservoirs. Vapor mole fraction above the evaporating droplet has been reported using different experimental techniques, i.e., IR absorption [20], digital holographic interferometry [21], interferometry [22], and planar laser-induced fluorescence (PLIF) [23]. Singh and Panigrahi used inline digital holography and particle tracking velocimetry to study the Taylor flow inside a microcapillary [24]. The vapor cloud analysis using digital holographic interferometry provides an accurate measure of vapor mole fraction distribution. However, no measurement of vapor cloud above a liquid well is available in the literature. The present study implements holographic interferometry for characterization of the vapor cloud outside the liquid well. Several earlier studies carried out for water droplets or flat circular disks have reported an analytical expression assuming diffusion-limited evaporation based on electrostatic analogy of a flat disk at constant potential [25]. Dehaeck *et al.* experimentally measured local evaporation rate and interfacial temperature of a suspended HFE-7100 droplet and observed that the measured vapor cloud differs from calculation based on a pure diffusion-controlled evaporation model [21].

Most of the studies in the literature have reported evaporation from droplets and circular reservoir wells using water as working fluid. Several analytical and simulation studies have assumed diffusion-limited evaporation. However, no study on evaporation from wells with high molecular weight liquid hydrocarbons is available. Correlations for estimation of the evaporation rate from droplets are available and there are no correlations for evaporation rate estimation from well geometries. It may be noted that hydrocarbon vapor is heavier than the surrounding gas (air) contrary to that of water vapor, which is lighter than surrounding air. Understanding the evaporation of such liquids from a reservoir is important since hydrocarbons can serve as reagents in various chemical reactions and as a cover film on the interface to control the evaporation of water from a reservoir due to insolubility of these liquids. The primary objective of the present study is to investigate the vapor phase transport above a liquid well during the evaporation of high molecular weight hydrocarbons. Gravimetric analysis is carried out for evaporation rate measurement and digital holographic interferometry is used for vapor concentration measurement inside the vapor cloud. New correlation is proposed for estimation of the evaporation rate from a circular well. A diffusion-limited simulation study is carried out and compared with experiments demonstrating the convection dominated evaporation process outside the well region.

2. EXPERIMENTAL DETAILS

The experimental study consists of two parts, i.e., measurement of the evaporation rate from the liquid well and holographic interferometry measurement of the concentration inside the vapor cloud. The details of the experimental arrangement are reported in the following section.

A. Evaporation Rate Measurement

Circular well cavities with a radius ranging from 1.5 to 12.5 mm and a depth of 2 mm have been used to study the effect of well radius on evaporation rate. Pentane, hexane, cyclohexane, and heptane are used as working fluids. These liquids are selected due to their wide range of volatility, nearly equal molecular weight (M), and latent heat of vaporization (ΔH). Important thermophysical properties of these working fluids are presented in Table 1. Vapor pressure (P_V) values are adopted from [26] and diffusion coefficient (D) values in air are taken from [27–29], at ambient temperature (T_{amb}) and pressure (P_{amb}) equal to $25 \pm 0.5°C$ and 1 atm, respectively. Diffusion coefficient values at ambient condition are computed according to the following equation [30]:

$$D = D_o \left(\frac{T}{T_o} \right)^2, \tag{1}$$

where D_o is the nominal value of the diffusion coefficient at a reference temperature T_o and T is the actual temperature. Values of ΔH at the normal boiling point (T_b) are adopted from [31]. Gravimetric analysis has been performed to measure the evaporation rate of liquid evaporating from the circular well.

Table 1. Thermophysical Properties of Working Fluids Used in the Present Study at Atmospheric Pressure and 25°C Temperature[a]

Liquid	P_v (kpa)	T_b (k)	M (g/mol)	D (m^2/s) x 10^{-6}	Density Ratio $(\frac{\rho_{mix}-\rho_a}{\rho_a})$	ΔH (J/kmol) x10^7	Grashof Number (Gr)	Saturated Concentration (C_s) (mol/m^3)
Pentane	68.394	309	72	8.4 [27]	0.986	2.58	141-82120	27.59
Hexane	20.265	342	86	8.2 [27]	0.387	2.88	56-32253	8.17
Cyclohexane	13.065	354	84	8.145 [28]	0.240	3	35-20066	5.27
Heptane	6.133	372	100	7.3 [29]	0.146	3.18	21-12158	2.47

[a]Vapor pressure (p_v) values are adopted from [26] and the reference sources for diffusion coefficient (D) are mentioned in the bracket.

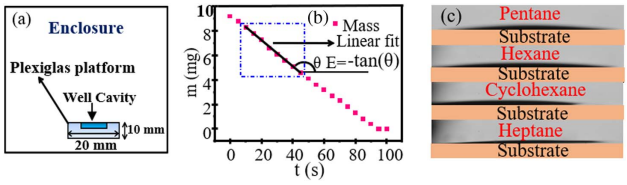

Fig. 1. (a) Schematic diagram of gravimetric measurement setup for evaporation rate measurement, (b) sample measurement data of liquid hydrocarbon mass (m) with time (t). A straight line fit over the range of 90% to 50% of the initial mass and its negative slope is used as a measure of evaporation rate. (c) Contact angle of 5 μl volume droplet of pentane, hexane, cyclohexane, and heptane on Plexiglas substrate.

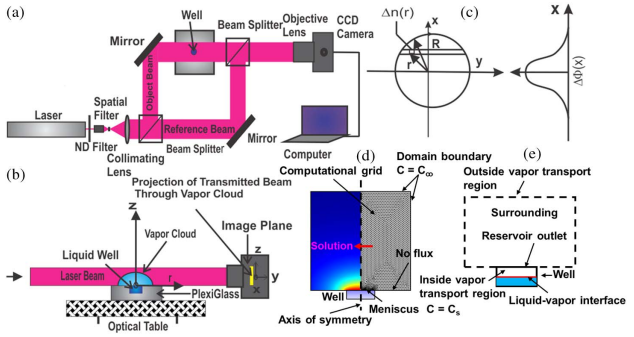

Fig. 2. (a) Schematic of digital holographic interferometry setup used to visualize the vapor cloud; (b) schematic showing the image formation and coordinate system; (c) cross section of the laser beam with nomenclature and recorded phase profile on the image plane; (d) schematic illustration of computational domain with boundary conditions and a sample simulation result; and (e) details of the vapor transport region during evaporation of liquid from the well.

Circular wells with a radius ranging from 1.5 to 10 mm were machined using a Plexiglas piece with a length and width equal to 20 mm and height of 10 mm. Wells with a bigger radius than 10 mm were machined on a Plexiglas piece of 30 mm length and width with 10 mm height. Non-conducting Plexiglas material and a larger size of reservoir body compared to the size of the well is selected such that the effect of heat transfer from the substrate is negligible. The liquid is filled inside the circular well with the help of a micropipette and the weight of the well is recorded with time by an analytical balance, having readability and repeatability of 0.1 mg.

A schematic of the setup for gravimetric analysis is shown in Fig. 1(a). The circular well cavity is placed on the pan of the analytical balance (OHAUS Adventurer Pro). The glass windows of the balance are closed to prevent influence of ambient air movement. The enclosed volume inside the glass enclosure is equal to 6311 cm^3. A sample plot of transient mass variation of pentane for a well radius of 1.5 mm is shown in Fig. 1(b) to illustrate the evaporation rate calculation procedure. The data till 90% of initial mass is neglected for evaporation rate calculation to avoid the influence of initial transients due to the effect of pouring and splashing of liquid above the surface of the well. A linear fit is performed from 90% to 50% of initial mass and negative of the slope is used as a measure of the evaporation rate [see Fig. 1(b)]. It may be noted that maximum 3% deviation is observed when using the linear fit from 90% to 30% of initial mass indicating insignificant influence of data range on evaporation rate calculation.

B. Digital Holographic Interferometry

The digital holographic interferometry technique is used for real-time measurement of shape, size, and vapor mole fraction inside the vapor cloud. It is a non-intrusive, line of sight technique which has been used for temperature [32] and concentration [21] measurements with high temporal and spatial resolution. In digital holography, an interference pattern is recorded on a CCD/CMOS sensor, which contains the information about phase difference with respect to an incoming wave due to temperature or concentration distribution. This interference pattern is called hologram. More details on off-axis digital holographic interferometry can be found in [33]. The layout of the experimental setup used for digital holographic interferometry is shown in Fig. 2(a). A He–Ne laser with a wavelength of 632.8 nm and 0.98 mm beam diameter is passed through the neutral density filter to adjust the intensity of the laser beam. Subsequently, it is spatially filtered using a spatial filter having a combination of a 40× microscope objective lens and 10 μm size pinhole. The spatially filtered beam is subsequently collimated by a collimating lens with a focal length equal to 15 cm. The collimated beam is passed through the first beam splitter which splits the beam into an object and reference beam. The object beam is one which transmits through the object of interest, i.e., the vapor cloud. The reference beam passes through the ambient air, and the two beams are recombined by the second beam splitter and imaged on a CCD camera (Basler, 782 × 582 pixe1^2 and resolution of 8.30 μm) with a maximum frame rate of 53 frames/s using a zoom lens (NAVITAR).

The inline holographic interferometry has been used to visualize the iso-concentration contours inside the vapor cloud

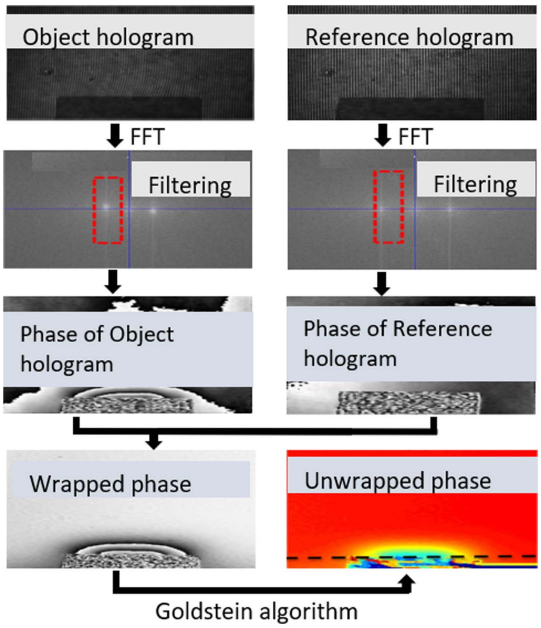

Fig. 3. Block diagram demonstrating the sequence of image processing steps used for extraction of the phase shift. A sample hologram image of the pentane evaporation experiment has been used as test data.

formed above the circular well cavity. A 2.5 mm radius circular well cavity is selected for the holographic visualization experiments. The digital holographic interferograms are used for calculation of vapor mole fraction distribution. Before filling the liquid inside the circular well cavity, the interferometer is set in wedge fringe setting by setting a small angle between the object beam and the reference beam. As a result, homogeneous vertical fringes with a finite carrier frequency (f_o) are formed on the camera. A reference hologram is recorded without filling the liquid inside the well cavity and stored in the computer attached with the CCD camera. A sample reference hologram has been shown in Fig. 3. The reference hologram helps to overcome the problem of aberrations produced by various types of optical elements in the recording setup. After filling of liquid inside the well, holograms are recorded at the interval of 1 s until liquid is fully evaporated from the well. A sample object hologram is shown in Fig. 3. The detailed procedure of data analysis for mole fraction distribution calculation is presented in the following section.

3. DATA ANALYSIS

The image processing of holographic interferograms has been carried out to obtain the phase distribution in the projected plane due to concentration variation in the vapor cloud. Subsequently tomographic reconstruction has been carried out to obtain the 3D distribution. The estimation of mass transfer assuming the diffusion-limited model has been carried out to estimate the role of free convective mass transfer. The detailed data analysis procedure is described in the following sections.

A. Digital Holographic Image Processing

The flow chart explaining the procedure for extracting useful phase information from the recorded holograms is shown in Fig. 3. The Fourier transform profilometry (FTP) [34] algorithm is used to extract the useful phase information from the holograms. The FTP algorithm is implemented in the MATLAB platform. As the interferometer is set in the wedge fringe setting in off-axis holography, such a type of fringe-pattern intensity distribution, $I(x, z)$, can be represented using the following equation [34]:

$$I(x, z) = b_1(x, z) + b_2(x, z)\cos[2\pi f_o x + \phi(x, z)], \quad \textbf{(2)}$$

where $b_1(x, z)$ and $b_2(x, z)$ represent unwanted irradiance variations arising from the non-uniform light reflection or transmission by the test object and the term $\phi(x, z)$ contains the desired phase information. The spatial variation of $b_1(x, z)$, $b_2(x, z)$, and $\phi(x, z)$ are slow compared to the spatial carrier frequency f_o. Therefore, the Fourier spectra of Eq. (2) are separated by the carrier frequency f_o. This can be clearly seen in the 2D Fourier spectrum calculated using the fast Fourier transform (FFT) algorithm of the object hologram and reference holograms shown in Fig. 3. One of the spectra at carrier frequency is selected and translated by f_o on the frequency axis toward the origin. Unwanted background variation $b_1(x, z)$ is filtered out in this stage. Subsequently, the inverse Fourier transform of the filtered spectrum is calculated, which provides a matrix of complex number at each pixel. The phase at each pixel is calculated by the arctan function of MATLAB which provides the principal value ranging from $-\pi$ to π. A sample phase map of object and reference holograms is shown in Fig. 3. The phase of the object hologram at each pixel is subsequently subtracted by the phase of the reference hologram at the same pixel by modulo 2π subtraction. This yields the total phase shift of each pixel at any arbitrary time and is known as the wrapped phase difference whose values are continuous between 0 and 2π. The following equation is used for calculating the wrapped phase $\Delta\phi_w$:

$$\Delta\phi_w(m, n) = \begin{Bmatrix} \phi_o(m, n) - \phi_r(m, n) & \text{if } \phi_o(m, n) \geq \phi_r(m, n) \\ \phi_o(m, n) + \phi_r(m, n) + 2\pi & \text{if } \phi_o(m, n) \leq \phi_r(m, n) \end{Bmatrix}, \quad \textbf{(3)}$$

where m and n denote the pixel location and ϕ_o and ϕ_r are the phase of the object and reference holograms, respectively. A sample wrapped phase map is shown in Fig. 3. This direct measurement of phase shift information indicates the advantage of digital holographic interferometry over classical holographic interferometry, where interference pattern analysis is needed to extract phase difference. The process of removing 2π discontinuities in the wrapped phase is known as phase unwrapping and the resulting phase distribution is continuous in the $x-z$ plane. The continuous phase distribution is called the unwrapped phase ($\Delta\phi$), which is shown in Fig. 3. The 2π phase discontinuity in the wrapped phase can be removed by integrating the wrapped phase differences [35]. Integration of phase gradients over a region needs two-dimensional phase unwrapping. If the integration depends on the path, then it gives different results for different paths leading to inconsistencies in the result. In order to tackle these inconsistencies, Goldstein *et al.* [36] proposed a new term called residues to find inconsistencies and avoid them using the Branch cut method. The details of the

phase unwrapping process by the Goldstein algorithm is discussed in [36]. The unwrapped phase shift is proportional to the change in the optical path length of the laser beam, which arises when the beam passes through the axisymmetric refractive index field surrounding the circular well cavity. The refractive index distribution in the object field is calculated using the tomographic reconstruction, which is presented in the following section.

B. Tomographic Reconstruction

The obtained unwrapped phase field provides the projected phase difference for each line of sight, perpendicular to the direction of propagation of the laser beam [see Figs. 2(b) and 2(c)]. This phase field is tomographically reconstructed to give a three-dimensional refractive index distribution (Δn). If the vapor cloud above the well cavity is axisymmetric (as experiments are performed in the quiescent environment in the closed enclosure), an inverse Abel inversion can be applied to the obtained unwrapped phase distribution, in the object plane expressed as [21]

$$\Delta n(r) = \frac{-\lambda}{2\pi^2}\int_r^\infty \frac{\Delta\phi'(x)}{\sqrt{(x^2-r^2)}}\mathrm{d}x. \tag{4}$$

Here, $\Delta n = (n_{\mathrm{mix}} - n_a)$, where n_{mix} denotes the refractive index of the air–vapor mixture and n_a is the refractive index of air at ambient temperature and pressure, r is the radial co-ordinate, λ is the wavelength of the laser beam, and $\Delta\phi'(x)$ is the first derivative of the unwrapped phase shift. The pictorial representation of the co-ordinate system used here is shown in Figs. 2(b) and 2(c). There are several algorithms available for solving the integral in Eq. (4), such as the three-point Abel inversion [37], Fourier–Hankel [38], and even polynomial methods [39]. The Fourier–Hankel method has been used in the present study as this method can greatly reduce the computation time by using the FFT algorithm and the singularity in the inverse Abel transform is also avoided due to the use of the analytical method. By taking the Fourier transform of the unwrapped phase and changing the variables of the integration to polar coordinates, it can be shown that the Fourier transform of $\Delta\phi(x)$ is equal to the zero-order Hankel transform of $\Delta n(r)$ at any given height z. Therefore, the refractive index distribution can be recovered from the inverse Hankel transform as follows [38]:

$$\Delta n(r) = \frac{\lambda}{2\pi^2}\int_0^\infty G(f) f J_o(fr)\mathrm{d}f, \tag{5}$$

$$J_o(fr) = \frac{2}{\pi}\int_0^\infty \sqrt{(x^2-y^2)}\mathrm{Sin}(fr)\mathrm{d}x, \tag{6}$$

where $G(f)$ is the continuous Fourier transform of the unwrapped phase, $J_o(fr)$ is the zero-order Bessel function of the first kind, and f denotes the frequency domain. Figure 4(a) shows a sample unwrapped phase map of pentane vapor evaporating from the circular well cavity and the corresponding 3D refractive index field is shown in Fig. 4(b). The obtained refractive index field can be converted into the vapor mole fraction field, χ, by using the Lorentz–Lorenz equation [40]. The relation between the refractive index difference field with local temperature, T, and mole fraction, χ, is given as [21]

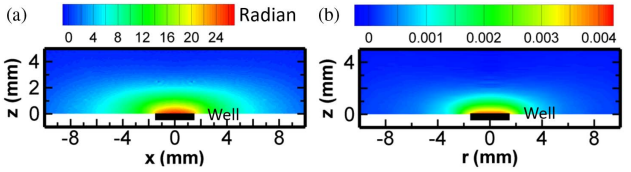

Fig. 4. (a) Unwrapped phase field and (b) corresponding refractive index field using Abel inversion algorithm of liquid pentane evaporating from the well of 1.5 mm radius.

$$\chi = \frac{1}{\Delta n_{\mathrm{ref}}}\frac{T}{T_{\mathrm{amb}}}\left[\Delta n - (n_a - 1)\left(\frac{T_{\mathrm{amb}}}{T} - 1\right)\right]. \tag{7}$$

Here, $\Delta n_{\mathrm{ref}} = (n_v - n_a)$, where n_v and n_a are the refractive index of pure vapor of liquid and air, respectively, at ambient temperature and pressure. It is not possible to extract the vapor mole fraction field using this relation without knowing local temperature, T. If the temperature impact is marginal, then it can be neglected by setting $T \approx T_{\mathrm{amb}}$ [21] and Eq. (7) can be simplified as

$$\chi = (\Delta n/\Delta n_{\mathrm{ref}}). \tag{8}$$

Local temperature non-uniformity at the liquid–vapor interface affects the refractive index field leading to the overestimation of vapor mole fraction by a few percent [21]. There is no dedicated gas refractometer available which can measure the refractive index of pure vapor of liquid for the wavelength of 632.8 nm at the ambient temperature of 25°C. The refractive index values of pure vapor of the working fluids are also not available in the literature. Therefore, the actual vapor mole fraction value cannot be calculated. Equation (8) indicates that vapor mole fraction is directly proportional to the refractive index change. Therefore, the refractive index map can be used directly as an indicator of vapor mole fraction distribution for characterization of vapor cloud.

C. Mass Transfer by Diffusion

The diffusion-limited evaporation rate of the liquid well using the diffusion-limited model is given as [41]

$$E_d = 4D(C_s - C_\infty)R, \tag{9}$$

where E_d is the diffusion-limited evaporation rate, D is the diffusion coefficient, C_s is the saturated concentration of vapor at the liquid–vapor interface, C_∞ is the vapor concentration far away from the well region, and R is the radius of the well. Equation (9) is valid for low Grashof number (Gr), and the Grashof number is defined as

$$Gr = \frac{\rho_a(\rho_{\mathrm{mix}} - \rho_a)g\,R^3}{{\mu_a}^2}. \tag{10}$$

The density difference, $\rho_{\mathrm{mix}} - \rho_a$ is calculated from the following relation:

$$(\rho_{\mathrm{mix}} - \rho_a) = \frac{P_{\mathrm{sat}}(T_{\mathrm{amb}})(M - M_a)}{R_u\,T_{\mathrm{amb}}}, \tag{11}$$

where ρ_a and ρ_{mix} are the density of ambient air and air–vapor mixture, respectively, g is the gravitational acceleration, R_u is

the universal gas constant, $P_{sat}(T_{amb})$ is the saturation pressure of the liquid at ambient temperature, μ_a is the dynamic viscosity of air at ambient temperature, and M and M_a are the molecular weight of evaporating species and air, respectively. The Grashof number for the range of well diameter and working fluids used in the present study varies between 21 and 82,119 indicating relative strength of natural convection. The range of Gr values for each working fluid is compiled in Table 1. Gr values for the small radius wells are small and higher values of Gr are encountered for higher well radius even for the least volatile fluid such as heptane.

D. Uncertainty Analysis

The error in gravimetric measurement of the evaporation rate is attributed to the error in the initial volume setting of liquid inside the well due to micropipette setting error, resolution of the electronic balance, fluctuation in ambient condition, and the disturbance due to natural convection in the surrounding medium. Experiments are conducted at least three times and the average values of multiple experiments are reported. The electronic balance used for gravimetric measurement is initialized to zero value at the beginning of each experiment. The least count of the electronic balance is 0.1 mg and therefore the contribution of bias error is insignificant in the evaporation rate measurement. Similarly, the reference intensity image is subtracted from the object field image for data analysis of the holographic interferograms. Therefore, any bias errors due to electronic noise or other environmental effects are eliminated during holographic data inversion. Maximum uncertainty of the evaporation rate based on gravimetric experiment is found to be within 6%. The error in the initial volume of liquid inside the well, convection inside the room, fluctuation of incident light, and image acquisition error can influence the holographic interferogram pattern. The same fringe pattern of the holographic interferogram was observed in repeated experiments. The maximum uncertainty in intensity value of the interferogram is observed to be equal to 5%. The uncertainty in vapor concentration distribution can be attributed to the fluctuation in intensity distribution, error propagation due to phase unwrapping, and tomographic inversion. The maximum uncertainty in vapor concentration from repeated measurements is observed to be equal to 9%.

4. RESULTS AND DISCUSSION

The evaporation process of circular well cavity configuration has been studied using four working fluids, i.e., pentane, hexane, cyclohexane, and heptane for a well radius ranging from 1.5 to 12.5 mm. Gravimetric measurements are carried out for obtaining the rate of evaporation. Holographic interferometry followed by tomographic analysis has been carried out for characterizing the concentration distribution of the vapor cloud. Simulation assuming diffusion-limited evaporation is carried out in the COMSOL Multiphysics platform. The existing correlations for evaporation rate estimation based on sessile droplet geometry have been evaluated for the circular well and a modified correlation has been proposed. The results from the present study are discussed in the following sequence: (a) digital holographic analysis of the vapor cloud, (b) rate of evaporation, (c) evaporation rate correlation, and (d) conceptual picture of the vapor cloud.

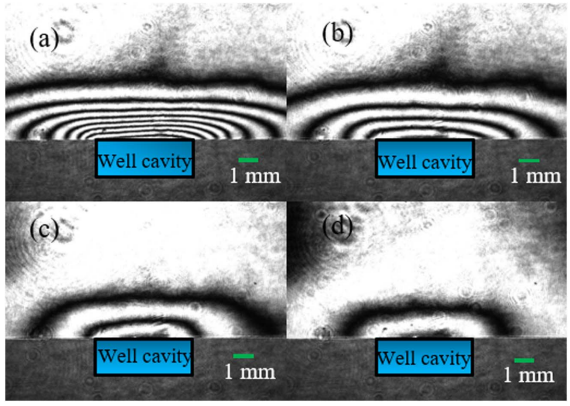

Fig. 5. Sample interferogram of vapor cloud over a liquid well of radius $R = 2.5$ mm during the initial period for different liquid hydrocarbons: (a) pentane, (b) hexane, (c) cyclohexane, and (d) heptane. The total duration of evaporation is equal to 1.2 min, 3.41 min, 14.08 min, and 18.633 min for pentane, hexane, cyclohexane, and heptane, respectively. The time is normalized with respect to the total evaporation time for respective fluids (see Visualization 1).

A. Digital Holographic Analysis of the Vapor Cloud

Digital holographic analysis reveals both spatial and transient behavior of the vapor cloud from evaporation of heavy hydrocarbons in the circular well cavity. The nature of the vapor cloud is correlated with the rate of evaporation. Figure 5 shows holograms representing iso-concentration lines of the vapor cloud from the well with a 2.5 mm radius. It shows that most volatile pentane contains the highest number of fringes and maximum spread compared to less volatile liquids such as hexane, cyclohexane, and heptane. The fringe spacing is minimum for pentane and maximum for least volatile heptane. Videos have been recorded from the beginning until the end of evaporation to visualize the dynamics of the vapor cloud. The video recordings provide insight into the temporal behavior of the evaporation process. These videos are included in the online version of the article (Fig. 5). It is found that a flat vapor cloud forms above the surface of the well, which remains steady until complete evaporation of the liquid. The shape of the vapor cloud extends radially outward from the well indicating the presence of natural convection in the radial outward direction. Since vapor produced is heavier than air, the gravity force opposes diffusion in the vertical direction. Kelly-Zion *et al.* [20,42] observed similar behavior of a vapor cloud for a sessile drop by Schlieren visualization and infrared tomography, respectively. They reported a flat-disk-shaped vapor cloud which differs from the prediction of the diffusion-limited evaporation model for a sessile drop.

1. *Comparison Between Experiment and Diffusion-Limited Model*

Experimentally measured vapor clouds are compared with the reference case of pure diffusion-limited evaporation to reveal

the strength of convection inside the vapor cloud. An axisymmetric numerical model is used to solve the steady-state Laplace equation using commercial software (COMSOL 5.3). The governing equation and respective boundary conditions are given below:

$$\nabla^2 C = 0, \tag{12}$$

$$C = C_s \text{ (At liquid air interface)}, \tag{13}$$

$$C = C_\infty \text{ (At away from well surface)}, \tag{14}$$

$$\nabla C = 0 \text{ (No flux at the wall)}. \tag{15}$$

Figure 1(c) shows the static contact angle of all hydrocarbons used in the present study on the Plexiglas surface. The static contact angles for all hydrocarbons are close to zero. The shape of the liquid–vapor interface inside the well is flat due to very small contact angle and shallow reservoir behavior. A constant saturation boundary condition is applied at the liquid–vapor interface. A domain which is 15 times larger than the well radius is used as the external boundary condition, where vapor concentration is zero.

Extra-fine triangular mesh with 4350 number of elements is used to represent the computational domain [see Fig. 2(d)]. The average and minimum mesh quality is equal to 0.988 and 0.774, respectively. As the interface moves below the well boundary, the concentration profile between the liquid–vapor interface and the top of the well cavity cannot be imaged by digital holography since the light cannot penetrate inside the well cavity. The holographic interferometry analysis provides vapor distribution above the top boundary of the well. Therefore, the experimental results in the initial period when the maximum displacement of liquid–air interface with respect to the initial height is less than 2% are compared with the diffusion-limited simulation results. Figure 6 shows the normalized vapor cloud concentration of liquid evaporating from the well cavity of 1.5 mm radius. Normalization is performed with respect to the maximum change in refractive index for the measured vapor cloud. The saturation concentration at the interface is used for normalization of the vapor cloud in simulation results. Table 1 presents the values of saturated concentration at the interface for all working fluids.

Figure 6 shows that the experimentally measured vapor cloud is a flat disk type with significant spread in the radial direction from the edge of the well. This may be attributed to the species transport due to radial convection. The vapor cloud from the diffusion-limited model is hemispherical in shape with greater spread in the normal direction, i.e., perpendicular to the interface of the well compared to the measured vapor cloud. The vapor cloud of heptane shows maximum flatness which can be attributed to its lowest density difference ratio. The maximum magnitude of vapor concentration is observed inside the vapor cloud of pentane while the minimum magnitude is found for heptane. It may be noted that heptane is least volatile, and the low rate of evaporation causes minimum change in refractive index for heptane.

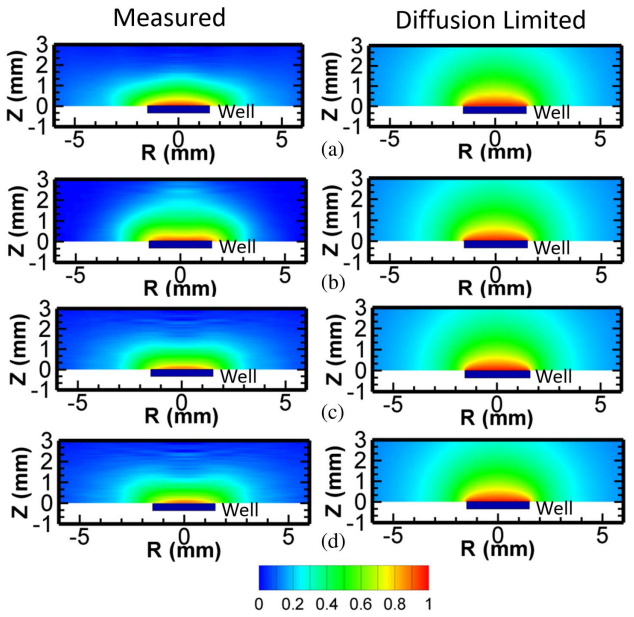

Fig. 6. Normalized vapor cloud concentration above the well. The left-hand side represents the measured vapor cloud during the initial period ($t \sim 0$) and the right-hand side represents the vapor cloud based on the pure diffusion-limited model for different working fluids.

Figure 7 presents normalized vapor concentration (C^*) variation in the normal direction ($z^* = z/R$) at the center of the well ($r = 0$) during the initial period of evaporation ($t \approx 0$). It may be observed that the measured vapor concentration diminishes to zero at a lower normal distance, z^*, compared to that of the diffusion-limited case. The vertical gradient of the measured concentration profile at the interface is comparatively higher for the experimental case in comparison to the diffusion-limited case. The higher concentration gradient indicates greater evaporation rate, which may be attributed to convection effects. The additional transport by convection enhances the evaporation compared to the pure diffusion of vapor. The slope of the concentration profile reduces at $z^* \geq 1$ location indicating lower density difference between the vapor cloud and ambient due to mixing.

Figure 8 shows the variation of normalized concentration (C^*) along the radial direction ($R^* = r/R$) at two different z locations, i.e., 180 μm (near the well boundary) and 1.5 mm above the well surface during the initial period of evaporation ($t \approx 0$). The radial distribution of the refractive index is almost similar to the diffusion-limited model near the interface region of the well. This may be attributed to the dominance of diffusion transport mechanism near the interface region. However, the experimentally measured concentration profile shows a larger deviation from that of the diffusion-limited model in the outer region of the vapor cloud, i.e., away from that of the well interface.

The average concentration is also higher compared to that of the diffusion-limited model. This behavior is attributed to secondary transport due to the convection of vapor in the radial direction. The surface plot shown as the inset in Fig. 8 and the comparison of the concentration profile between $z = 180$ μm

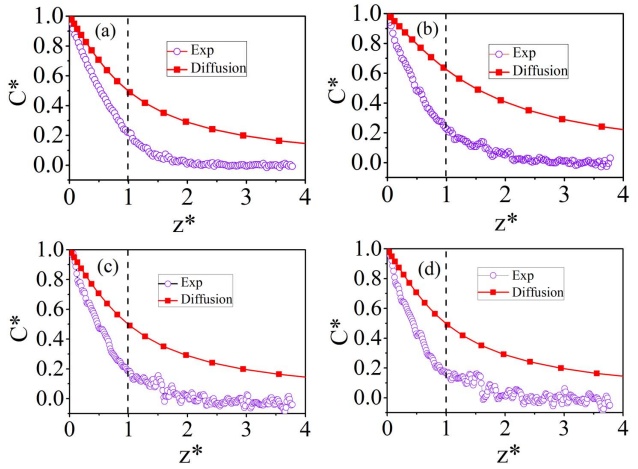

Fig. 7. Variation of normalized vapor concentration, where Co is the concentration at the center of the well ($r = 0$) in normal direction ($z^* = z/R$) from the experiment during the initial time period and diffusion-limited calculation for different liquid hydrocarbons: (a) pentane, (b) hexane, (c) cyclohexane, and (d) heptane.

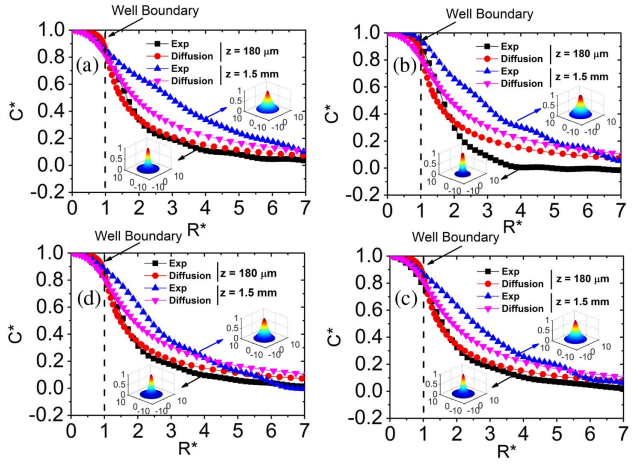

Fig. 8. Normalized vapor concentration ($C^* = C/\mathrm{Co}$) profile in the radial direction ($R^* = r/R$) at $z = 180$ μm and $z = 1.5$ mm above the well surface from the experiment during the initial period of evaporation ($t \approx 0$) and diffusion-limited model for different liquid hydrocarbons (contour maps shown are from experimental results).

and $z = 1.5$ mm indicate lower spread of concentration distribution in the near wall region compared to the outer region possibly due to viscous effects.

The normalized vapor mole fraction profile at the liquid–air interface (Fig. 8) shows that vapor concentration decreases from the center region toward the edge of the well. From the measured concentration field, the local evaporation rate can be estimated using the following equation [21]:

$$J = -\frac{MP_{\mathrm{amb}}D}{RT_{\mathrm{amb}}(1-\chi_\sigma)}\left.\frac{\partial \chi}{\partial z}\right|_{z=0}. \tag{16}$$

Here, χ_σ is the vapor mole fraction at the interface and $\frac{\partial \chi}{\partial z}|_{z=0}$ is a normal gradient of mole fraction at the interface. All other terms in Eq. (16) are constants except the mole fraction

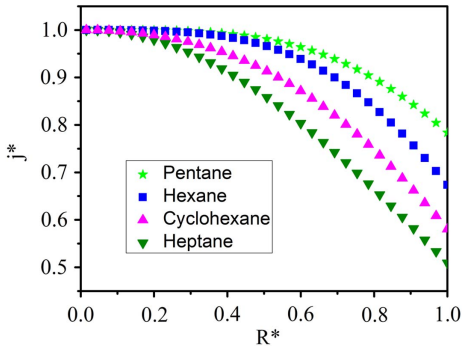

Fig. 9. Normalized local evaporation rate (j^*) variation in the radial direction ($R^* = r/R$) on the liquid–vapor interface of the liquid well ($z = 0$) for different hydrocarbons.

gradient at the interface indicating that the local evaporation rate is a function of normal mole fraction gradient at the interface. It is known that the mole fraction χ is directly proportional to the refractive index change Δn [Eq. (8)]. Therefore, the normal gradient of refractive index change at the interface can be used as a measure of local evaporation rate. The central difference method for calculating the gradient of refractive index at the interface gives noisy results. Therefore, a linear fit in the interface region—dominated by diffusion—is performed and the slope of the linear fit is used as a measure of evaporation rate. Figure 9 shows the normalized local evaporation rate (j^*) at the liquid–air interface of the well in the radial distance (R^*). Normalization is performed by dividing the local evaporation rate with the maximum evaporation rate at the center of the well interface. The normalized local evaporation rate decreases from the center of the well toward the edge of the well. The radial variation of the local evaporation rate is maximum for heptane and minimum for pentane. This behavior may be attributed to the vapor pressure difference between the working fluids, i.e., heptane has the lowest vapor pressure and pentane has the highest vapor pressure (see Table 1). The difference in the diffusivity between the working fluids is not significant compared to the vapor pressure difference.

2. *Temporal Behavior of the Vapor Cloud*

The temporal behavior of vapor distribution above the outlet boundary of the well cavity is helpful in explaining the dynamics of the evaporation process from the well cavity. Figure 10 shows the temporal variation of refractive index, i.e., the vapor mole fraction profile inside the vapor cloud near the outlet of the well cavity (at $z = 180$ μm) in the radial direction. The vapor mole fraction at the centerline of the well ($R^* = 0$) is maximum for pentane and minimum for heptane. This behavior correlates with the vapor pressure of the liquid (see Table 1). The average magnitude of vapor concentration within the vapor cloud reduces with time. This may be attributed to the drop of height of the liquid–air interface inside the well. The concentration gradient variation in the radial direction is small in the centerline region ($R^* < 1$) followed by a strong radial variation until $R^* = 2$ during evaporation. The concentration gradient is small in the $R^* > 2$ region, i.e., near the edge of the cloud. The maximum drop in concentration of the vapor cloud is observed in the

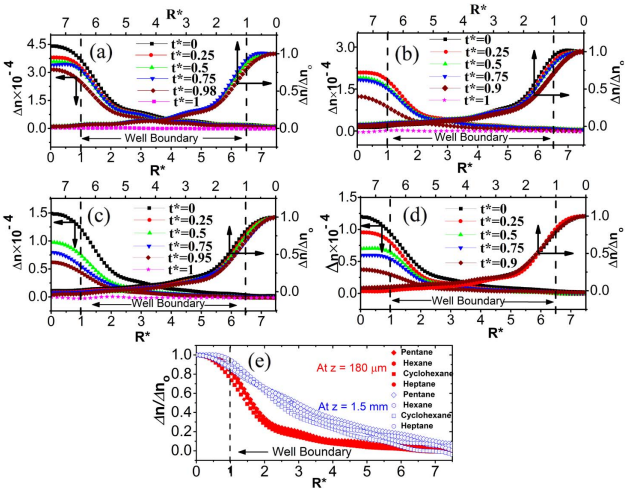

Fig. 10. Variation of change in the refractive index (Δn) in the radial direction ($R^* = r/R$) at wall normal location $z = 180$ μm for different normalized time, where te is the total time of evaporation and corresponding normalized refractive index ($\Delta n/\Delta n_o$) for different liquid hydrocarbons: (a) pentane, (b) hexane, (c) cyclohexane, and (d) heptane. The combined plot of the normalized concentration profile at all time instants and for all fluids at two z locations are shown in (e).

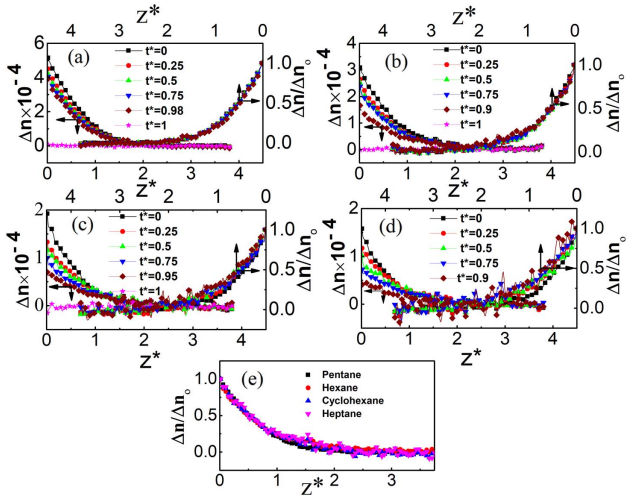

Fig. 11. Refractive index (Δn) profile in the normal direction ($z^* = z/R$) at the center of the well ($r = 0$) for different normalized time instants ($t^* = t/te$) and corresponding normalized refractive index ($\Delta n/\Delta n_o$) for different liquid hydrocarbons: (a) pentane, (b) hexane, (c) cyclohexane, and (d) heptane. The normalized concentration profile at all time instants and for all fluids are shown in (e) to demonstrate the universal nature of the evaporation phenomena.

centerline region ($R^* \approx 0$) at all times. This may be attributed to lower viscous effect offered by the sidewall of the well on the vapor movement from the liquid–air interface.

Figure 10 shows the normalized mole fraction ($\Delta n/\Delta n_o$) at different normalized times, where Δn_o is the refractive index value at the centerline. The overlap of the normalized concentration profile at all time instants indicates the invariant nature of vapor cloud mole fraction distribution with time at $z = 180$ μm. Figure 10(e) presents the time-averaged profile of the normalized refractive index in the normalized radial direction for all working fluids at $z = 180$ μm and $z = 1.5$ mm above the well boundary, respectively. The normalized profile overlaps at all time instants and for all working fluids at $z = 180$ μm. However, some deviation is observed at $z = 1.5$ mm, which may be attributed to the greater role played by the convection process away from the liquid–air interface.

Figure 11 shows the temporal variation of change in the refractive index profile, i.e., the vapor mole fraction along the normal direction (z^*) at the center of the well ($r = 0$) for various working fluids. Normalized vapor mole fraction plot with respect to the interface value ($\Delta n/\Delta n_o$) has been shown in the RHS for all working fluids. The height of the cloud remains constant with time and is approximately equal to $2.25 * R$ for all liquids. Normalized vapor mole fraction plots with time [see Fig. 11(e)] indicate the similar nature of vapor mole fraction distribution at the centerline of the well with time in the normal direction for all working fluids. The average vapor mole fraction varies within the cloud, based on the volatility of the liquid. Dynamics of the vapor cloud for liquid hydrocarbons whose vapor is heavier than the surrounding air shows similar behavior despite having different volatilities.

Figure 12 presents the measured evaporation rate, E_m, as a function of size of the well, i.e., well radius. The evaporation

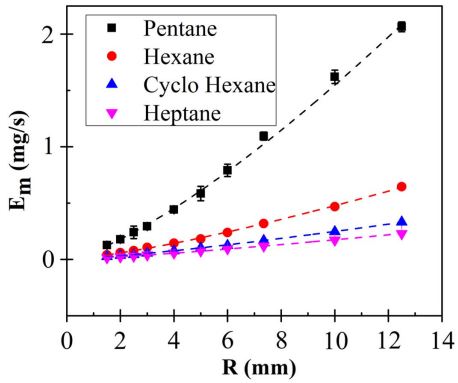

Fig. 12. Variation of measured evaporation rate (Em) as a function of size of the liquid well (R). Dotted line indicates the power law $Em = a\,R^b$ fit where a and b are constants.

rate strongly depends on both volatility of liquid and size of the well. Among the working fluids, pentane is most volatile, and its vapor pressure is more than 11 times higher than that of heptane. Therefore, the evaporation rate is highest for pentane and lowest for heptane for all well sizes. The rate of increase in evaporation rate with radius is also highest for pentane. The measured evaporation rate is fitted with a power series approximation between the measured evaporation rate and well radius, i.e., $E_m = a\,R^b$, where a and b are fitting constants. Exponent b of the fitted curve is 1.35 for pentane, 1.28 for hexane, 1.24 for cyclohexane, and 1.29 for heptane. It may be noted that Kelly-Zion *et al.* [13] observed the value of the exponent to be equal to 1.37 for a heptane sessile droplet. The lower value of the exponent for the well observed in the present study may be attributed to difference in the evaporation process due to the presence of the sidewall of the well.

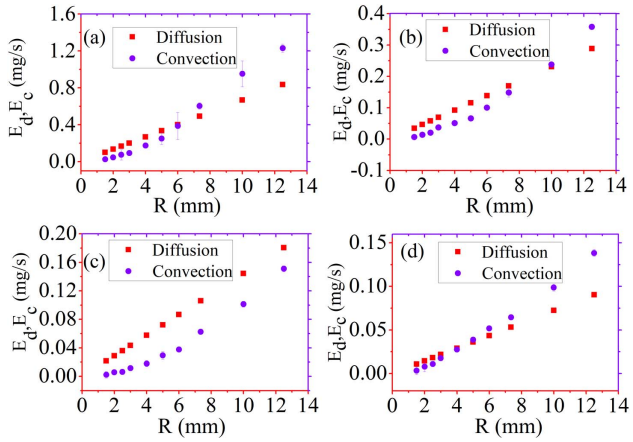

Fig. 13. Diffusion-limited evaporation rate (E_d) and convective part of evaporation rate (E_c) as a function of well radius (R) for different liquid hydrocarbons: (a) pentane, (b) hexane, (c) cyclohexane, and (d) heptane.

Previous studies on evaporation of sessile droplets [12,13] have estimated the influence of natural convection on the evaporation rate, with an assumption that the rate of vapor transport by convection and diffusion are independent of each other. The total evaporation rate is the sum of diffusion and convection contribution. The convective part contribution is estimated by subtracting the diffusion-limited evaporation from the measured evaporation rate. The same analogy has been used here for calculating the contribution of convection on the evaporation rate (E_c), which is equal to the difference between the measured evaporation rate and the diffusion-limited evaporation rate.

Figure 13 presents the diffusion-limited and convective contribution of the evaporation rate as a function of well radius. The convective motion contribution on the evaporation rate of all working fluids is small compared to the diffusion contribution for a small sized well. The contribution of the convective evaporation rate increases with an increase in well radius and is higher than the diffusion contribution after a critical well radius. Similar behavior was observed for hydrocarbons in the case of a sessile droplet [12]. It may be noted that the Grashof number value increases with increase in the size of the well (see Table 1) indicating a greater role of natural convection for a large sized well. The net evaporation rate from the hydrocarbons depends on the saturation concentration value and the combined resistance offered by the diffusion and convection process inside the vapor cloud. The diffusion resistance depends upon the mass diffusivity of the vapor. The convection resistance depends on the density ratio and Grashof number, which is a function of the diameter of the well. All these parameters do not vary monotonically for different types of hydrocarbon. Hence, it is expected that the relative diffusion and convection contribution on the vapor cloud will not have a similar trend for all working fluids. Figure 13 demonstrates the complexity of the transport process inside the vapor cloud above a well containing liquid hydrocarbon.

The fluids used in the current study have vapors which are heavier than air (surrounding medium). Therefore, the diffusion of vapor in the normal direction to the well surface is opposed by gravity and radially outward buoyancy induced convective flow is established. This behavior is analogous to natural convection heat transfer from a horizontal cold surface facing upwards, where surrounding air becomes heavier after coming in contact with the upward-facing cold surface and buoyancy induced radially outward convection is initiated. The natural convection in the vapor phase influences the evaporation rate and therefore the diffusion-limited model can no longer be used for evaporation rate estimation. Hence, there is a need for developing a new correlation for estimation of the evaporation rate for high molecular weight hydrocarbons from a circular well. The discussion on the development of correlation for the estimation of evaporation rate from a well is presented in the following section.

B. Evaporation Rate Correlation

Previous studies [12,13] have reported the correlation for evaporation of sessile droplets. The applicability of these correlations for a circular well cavity needs to be evaluated due to the difference in curvature of the liquid–air interface and effect of the sidewall of the well. Few studies are available for evaporation of sessile droplets of liquid hydrocarbons, where vapors are heavier than the surrounding medium. Kelly-Zion *et al.* [13] have developed the empirical model for sessile droplets for a broad range of volatilities and drop sizes given as

$$E = \frac{4dMP_v}{R_u T_{\text{amb}}}\left\{1 + 0.310\left[\frac{P_v Mg}{(P_{\text{amb}} - P_v)\, M_a \nu_a{}^2}\right]^{0.216} R^{0.648}\right\}, \tag{17}$$

where,

$$Z = \frac{P_{\text{amb}}}{P_v}\ln\left(\frac{1}{1-(P_v/P_a)}\right).. \tag{18}$$

Here, E is the evaporation rate, Z is the diffusion correction factor, and ν_a is the kinematic viscosity of air. Kelly-Zion *et al.* [12] also developed a modified correlation for the evaporation of sessile droplets based on the experiments conducted for eight different liquids having a wide range of volatility, molecular mass, and mass diffusivity. This correlation is different from the previously developed correlations in the sense that it contains specific non-dimensional terms which represent the influence of natural convection on the evaporation rate as

$$Sh = Sh_D + (0.345/\text{Pr}^{0.229}) \times ((\rho_{\text{mix}} - \rho_a)/\rho_a)^{-0.052} Sc^{0.508} Ra^{0.229}, \tag{19}$$

where Sh is the Sherwood number, Sh_D is the Sherwood number for diffusion-limited evaporation rate, Pr is the Prandtl number, Sc is the Schmidt number, and Ra is the Rayleigh number. The density difference ratio $(\rho_{\text{mix}} - \rho_a/\rho_a)$ is an additional term introduced to represent the effect of density difference. Here, the Sherwood number is expressed as

$$Sh = (h_m R/D) = (ER_u T/\pi R D P_v M), \tag{20}$$

$$Ra = Gr\ \text{Pr}. \tag{21}$$

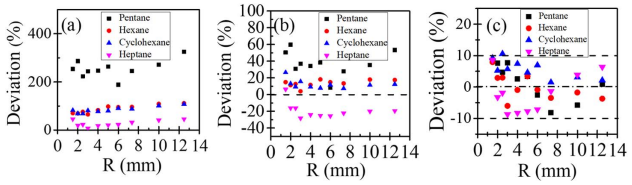

Fig. 14. Percentage deviation $((E_{com} - E_m)/E_m)$ using previously published correlation for sessile droplet and proposed new correlation: (a) computed using Eq. (17), (b) computed using Eq. (19), and (c) computed using the proposed correlation in Eq. (22).

Here, h_m is the mass transfer coefficient. The measured evaporation rate is used for calculating Sh and the diffusion-limited evaporation rate is used for calculating Sh_D. Results of previous correlations developed for sessile droplets, i.e., Eqs. (17) and (19) are compared with the measured evaporation rate for the circular well cavity. Figures 14(a) and 14(b) show the percentage error $((E_{com} - E_m)/E_m)$ between the computed evaporation rates (E_{com}) from Eqs. (17) and (19) and measured evaporation rates of the circular well cavity. As shown in Fig. 14(a), Eq. (17) always overestimates the evaporation rate and this overestimation is highest ($\cong 200\%$) for pentane which is the most volatile, and $\approx 50\%$ for hexane and cyclohexane and between 7% to 43 % for heptane.

Results obtained from Eq. (19) are presented in Fig. 14(b), which shows the computed evaporation rate overestimates the evaporation rate for pentane, hexane, and cyclohexane but under predicts the evaporation rate of heptane. The error in evaporation rate prediction is about 40% for pentane and about 30% for heptane. Overall, both the correlations developed for sessile droplets are not applicable in the liquid well configuration. Hence, a new correlation is proposed using the measured evaporation rate data of the circular well cavity which is as follows:

$$Sh = Sh_D + (c/\mathrm{Pr}^{n_3})((\rho_{mix} - \rho_a)/\rho_a)^{(n_1-n_2)} Sc^{n_2} Ra^{n_3} Z^{n_4}. \quad (22)$$

The density difference ratio introduces the natural convection effect and the effect of diffusivity is introduced by Sc in the equation. Since the working fluids have a wide range of volatility (vapor pressure), its effect is introduced by the diffusion correction factor (Z) in the correlation. The coefficients n_1, n_2, n_3, n_4, and c are fitting parameters which introduce the relative effect of different factors responsible for evaporation. The Ra values ranges between 14–58,058 and Sc ranges from 1.80–2.08. Nonlinear regression analysis is performed using the educational version of Polymath 6.0 software to compute fitting parameters. Values of correlation constants, i.e., n_1, n_2, n_3, n_4, and c, are equal to 0.767, 9.31, 0.224, −0.59, and 8.42×10^{-4}, respectively. Figure 14(c) shows the percentage difference between the evaporation rates computed from the proposed new correlation [Eq. (22)] and the measured evaporation rate. It may be observed that the new correlation successfully predicts the evaporation rate within 5.6% RMS error for a broad range of operating conditions, i.e., fluid type and size of the well.

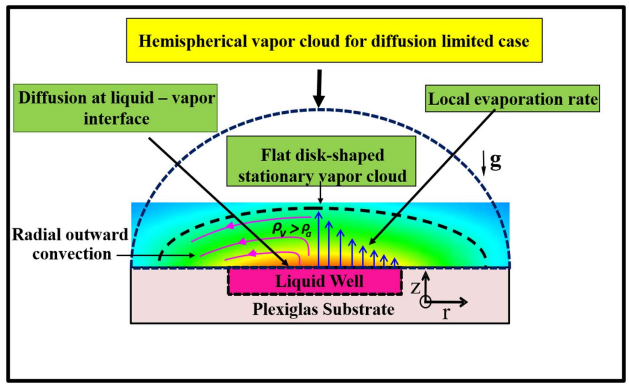

Fig. 15. Pictorial representation of the transparent phenomena of the vapor cloud due to evaporation from a liquid well.

C. Conceptual Picture of the Vapor Cloud

Figure 15 shows the schematic of the transport process in vapor phase during the evaporation of heavy hydrocarbons from a circular well cavity. The vapor cloud above the well is flat disk shaped compared to the hemispherical vapor cloud of a diffusion-controlled system. The evaporation flux on the well interface is maximum at the center of the well, which diminishes toward the edge of the well. Vapors of the working fluids are denser than air, which produces a vapor–air mixture heavier than the ambient air. Gravitational force opposes the flow of vapor away from the well interface, leading to formation of a stable vapor cloud. The vapor flux diffuses inside the ambient air leading to formation of a heavier vapor cloud. The heavier vapor cloud diffuses in the radial direction to maintain the mass continuity. The concentration gradient near the liquid interface increases due to additional transport by convection. As a result, the evaporation rate is enhanced compared to the diffusion-limited model. The strength of radial convection is proportional to the circumference of the liquid well. As a result, the deviation from diffusion-limited evaporation increases with an increase in the size of the well.

5. CONCLUSIONS

The evaporation dynamics of hydrocarbons from a circular well cavity is investigated using holographic interferometry and gravimetric evaporation rate measurements. Four working fluids i.e., pentane, hexane, cyclohexane, and heptane, are used, and the size of the circular wells is varied with the radius ranging from 1.5 to 12.5 mm. Phase unwrapping and tomographic reconstruction using the Fourier–Hankel method is used to reconstruct the concentration distribution inside the vapor cloud. A simulation study has been carried out in the COMSOL Multiphysics platform using the diffusion-limited evaporation model. Important findings of the current study are summarized as follows:

- Evaporation of volatile hydrocarbons from the circular well cavity of small depth does not follow the quasi-steady, diffusion-controlled evaporation model. The difference between the actual evaporation rate and the diffusion-limited model based evaporation rate is attributed to the secondary

transport mechanism due to natural convection occurring inside the vapor cloud.

- A flat, disk-shaped vapor cloud is formed above the circular well which is different from the hemispherical vapor cloud shape based on the pure diffusion-limited model. The downward convective flow pushes the vapor radially outward from the center region of the well.
- The gradient of the vapor mole fraction at the liquid–vapor interface is higher as compared to the diffusion-limited case due to the natural convection effect. The local evaporation rate along the well radius decreases from the center of the well toward the edge of the well due to the sidewall effect.
- The temporal behavior of the vapor cloud indicates the similar nature of vapor mole fraction distribution in the radial direction at all time instants near the liquid–air interface for all liquid hydrocarbons.
- The existing correlation for predicting the evaporation rate based on sessile droplets is not applicable for the circular well. A new correlation has been proposed for predicting the evaporation rate from the circular well cavity which successfully predicts the evaporation rate with a maximum RMS error of 5.6%.

Funding. Ministry of Electronics and Information Technology, Government of India.

Disclosures. The authors declare no conflicts of interest.

REFERENCES

1. M. Aghvami and A. Faghri, "Analysis of flat heat pipes with various heating and cooling configurations," Appl. Therm. Eng. **31**, 2645–2655 (2011).
2. K. S. Elvira, X. C. I. Solvas, R. C. Wootton, and A. J. Demello, "The past, present and potential for microfluidic reactor technology in chemical synthesis," Nat. Chem. **5**, 905–915 (2013).
3. C. Situma, M. Hashimoto, and S. A. Soper, "Merging microfluidics with microarray-based bioassays," Biomol. Eng **23**, 213–231 (2006).
4. Y. H. Lin, C. H. Chiang, M. H. Wu, T. M. Pan, J. D. Luo, and C. C. Chiou, "Solid-state sensor incorporated in microfluidic chip and magnetic-bead enzyme immobilization approach for creatinine and glucose detection in serum," Appl. Phys. Lett. **99**, 253704 (2011).
5. S. Morris, "The evaporating meniscus in a channel," J. Fluid Mech. **494**, 297–317 (2003).
6. C. T. Chen, F. G. Tseng, and C. C. Chieng, "Evaporation evolution of volatile liquid droplets in nanoliter wells," Sens. Actuators, A **130**, 12–19 (2006).
7. R. Moerman, J. Knoll, C. Apetrei, L. R. van den Doel, and G. W. van Dedem, "Quantitative analysis in nanoliter wells by prefilling of wells using electrospray deposition followed by sample introduction with a coverslip method," Anal. Chem. **77**, 225–231 (2005).
8. C. D. Bratten, P. H. Cobbold, and J. M. Cooper, "Micromachining sensors for electrochemical measurement in subnanoliter volumes," Anal. Chem. **69**, 253–258 (1997).
9. F. Carle, S. Semenov, M. Medale, and D. Brutin, "Contribution of convective transport to evaporation of sessile droplets: empirical model," Int. J. Therm. Sci. **101**, 35–47 (2016).
10. M. R. Barmi and C. D. Meinhart, "Convective flows in evaporating sessile droplets," J. Phys. Chem. B **118**, 2414–2421 (2014).
11. S. Somasundaram, T. Anand, and S. Bakshi, "Evaporation-induced flow around a pendant droplet and its influence on evaporation," Phys. Fluids **27**, 112105 (2015).
12. P. Kelly-Zion, J. Batra, and C. J. Pursell, "Correlation for the convective and diffusive evaporation of a sessile drop," Int. J. Heat Mass Transfer **64**, 278–285 (2013).
13. P. Kelly-Zion, C. Pursell, S. Vaidya, and J. Batra, "Evaporation of sessile drops under combined diffusion and natural convection," Colloids Surf. A **381**, 31–36 (2011).
14. J.-L. Marié, T. Tronchin, N. Grosjean, L. Méès, O. C. Öztürk, C. Fournier, B. Barbier, and M. Lance, "Digital holographic measurement of the Lagrangian evaporation rate of droplets dispersing in a homogeneous isotropic turbulence," Exp. Fluids **58**, 11 (2017).
15. K. T. Hjelt, R. van den Doel, W. Lubking, and M. J. Vellekoop, "Measuring liquid evaporation from micromachined wells," Sens. Actuators, A **85**, 384–389 (2000).
16. N. S. Lynn, C. S. Henry, and D. S. Dandy, "Evaporation from microreservoirs," Lab Chip **9**, 1780–1788 (2009).
17. L. R. van den Doel and L. J. van Vliet, "Temporal phase-unwrapping algorithm for dynamic interference pattern analysis in interference-contrast microscopy," Appl. Opt. **40**, 4487–4500 (2001).
18. T. K. Pradhan and P. K. Panigrahi, "Influence of an adjacent droplet on fluid convection inside an evaporating droplet of binary mixture," Colloids Surf. A **500**, 154–165 (2016).
19. T. K. Pradhan and P. K. Panigrahi, "Hydrodynamics of two interacting liquid droplets of aqueous solution inside a microchannel," Langmuir **34**, 4626–4633 (2018).
20. P. Kelly-Zion, C. J. Pursell, N. Hasbamrer, B. Cardozo, K. Gaughan, and K. Nickels, "Vapor distribution above an evaporating sessile drop," Int. J. Heat Mass Transfer **65**, 165–172 (2013).
21. S. Dehaeck, A. Rednikov, and P. Colinet, "Vapor-based interferometric measurement of local evaporation rate and interfacial temperature of evaporating droplets," Langmuir **30**, 2002–2008 (2014).
22. G. Toker and J. Stricker, "Holographic study of suspended vaporizing volatile liquid droplets in still air," Int. J. Heat Mass Transfer **39**, 3475–3482 (1996).
23. A. Charogiannis and F. Beyrau, "Laser induced phosphorescence imaging for the investigation of evaporating liquid flows," Exp. Fluids **54**, 1518 (2013).
24. D. K. Singh and P. Panigrahi, "Three-dimensional investigation of liquid slug Taylor flow inside a micro-capillary using holographic velocimetry," Exp. Fluids **56**, 6 (2015).
25. A. Gauss, *Fuel and Hydrocarbon Vaporization* (Army Ballistic Research Lab, 1973).
26. C. Yaws, *Thermodynamic and Physical Property Data* (Gulf Publication, 1992).
27. K. Beverley, J. Clint, and P. I. Fletcher, "Evaporation rates of pure liquids measured using a gravimetric technique," Phys. Chem. Chem. Phys. **1**, 149–153 (1999).
28. G. M. Cummings and A. Ubbelohde, "Collision diameters of flexible hydrocarbon molecules in the vapour phase: the 'hydrogen effect'," J. Chem. Soc. 3751–3755 (1953).
29. G. M. Cummings, E. McLaughlin, and A. Ubbelohde, "Collision parameters of C6—C9 hydrocarbons in the vapour phase: the hydrogen effect," J. Chem. Soc. 1141–1144 (1955).
30. G. Lugg, "Diffusion coefficients of some organic and other vapors in air," Anal. Chem. **40**, 1072–1077 (1968).
31. D. G. Friend, B. E. Poling, G. H. Thomson, T. E. Daubert, and E. Buck, *Physical and Chemical Data, Section 2* (McGraw-Hill, 2007).
32. V. Kumar, M. Kumar, and C. Shakher, "Measurement of natural convective heat transfer coefficient along the surface of a heated wire using digital holographic interferometry," Appl. Opt. **53**, G74–G83 (2014).
33. T. Kreis, *Handbook of Holographic Interferometry: Optical and Digital Methods* (Wiley, 2006).
34. M. Takeda, H. Ina, and S. Kobayashi, "Fourier-transform method of fringe-pattern analysis for computer-based topography and interferometry," J. Opt. Soc. Am. **72**, 156–160 (1982).
35. K. Itoh, "Analysis of the phase unwrapping algorithm," Appl. Opt. **21**, 2470 (1982).
36. R. M. Goldstein, H. A. Zebker, and C. L. Werner, "Satellite radar interferometry: two-dimensional phase unwrapping," Radio Sci. **23**, 713–720 (1988).
37. C. J. Dasch, "One-dimensional tomography: a comparison of Abel, onion-peeling, and filtered backprojection methods," Appl. Opt. **31**, 1146–1152 (1992).

38. S. Ma, H. Gao, and L. Wu, "Modified Fourier-Hankel method based on analysis of errors in Abel inversion using Fourier transform techniques," Appl. Opt. **47**, 1350–1357 (2008).
39. H. Chehouani, "A simple Abel inversion method of interferometric data for temperature measurement in axisymmetric medium," Opt. Laser Eng. **50**, 336–344 (2012).
40. A. Börzsönyi, Z. Heiner, M. Kalashnikov, A. Kovács, and K. Osvay, "Dispersion measurement of inert gases and gas mixtures at 800 nm," Appl. Opt. **47**, 4856–4863 (2008).
41. B. Dollet and F. Boulogne, "Natural convection above circular disks of evaporating liquids," Phys. Rev. Fluids **2**, 053501 (2017).
42. P. L. Kelly-Zion, C. J. Pursell, R. S. Booth, and A. N. VanTilburg, "Evaporation rates of pure hydrocarbon liquids under the influences of natural convection and diffusion," Int. J. Heat Mass Transfer **52**, 3305–3313 (2009).